small methods
www.small-methods.com

Specific Targeting and Imaging of RNA G-Quadruplex (rG4) Structure Using Non-G4-Containing L-RNA Aptamer and Fluorogenic L-Aptamer

*Hill Lam Lau, Haizhou Zhao, Hengxin Feng, and Chun Kit Kwok**

RNA G-quadruplex structures (rG4s) play important roles in the regulation of biological processes. So far, all the L-RNA aptamers developed to target rG4 of interest contain G4 motif itself, raising the question of whether non-G4-containing L-RNA aptamer can be developed to target rG4. Furthermore, it is unclear whether an L-Aptamer-based tool can be generated for G4 detection in vitro and imaging in cells. Herein, a new strategy is designed using a low GC content template library to develop a novel non-G4-containing L-RNA aptamer with strong binding affinity and improved binding specificity to rG4 of interest. The first non-G4-containing L-Aptamer, L-Apt.1-1, is identified with nanomolar binding affinity to amyloid precursor protein (APP) D-rG4. L-Apt.1-1 is applied to control APP gene expression in cells via targeting *APP* D-rG4 structure. Moreover, the first L-RNA-based fluorogenic bi-functional aptamer (FLAP) system is developed, and L-Apt.1-1_Pepper is engineered for in vitro detection and cellular imaging of *APP* D-rG4. This work provides an original approach for developing non-G4-containing L-RNA aptamer for rG4 targeting, and the novel L-Apt.1-1 developed for APP gene regulation, as well as the L-Apt.1-1_Pepper generated for imaging of APP rG4 structure can be further used in other applications in vitro and in cells.

1. Introduction

Guanine (G)-rich sequences in DNA and RNA can form into nucleic acid structure motifs referred to as G-quadruplex (G4) structures, which are assembled by two or more G-tetrads that are connected by loop nucleotides, and further stabilized by monovalent cations ($K^+ > Na^+ > Li^+$) (**Figure 1A,B**).[1–3] RNA G-quadruplexes (rG4s) are typically in parallel topology (Figure 1B), and a number of studies suggested that they can be detected in different classes of RNA[3–8] such as messenger RNAs (mRNAs), long non-coding RNAs (lncRNAs), microRNAs (miRNAs), transfer RNAs (tRNAs), and more. In addition, functional rG4s are reported in diverse organisms[3–8] including human, mouse, plants, bacteria, and others, highlighting their fundamental importance in biology across the tree of life. rG4s have been demonstrated to play roles in many biochemical processes, including regulation of transcription, RNA splicing, and translation, as well as control of RNA turnover and mRNA targeting.[3–8] From transcriptome-wide and transcript-specific studies,[9–11] we have previously identified and characterized a parallel rG4 at the 3'-untranslated region (3'-UTR) of *APP* mRNA (Figure 1B), and revealed the inhibitory role of *APP* 3'UTR rG4 on APP translation.[10,11] Amyloid precursor protein (APP) is an integral membrane protein that is commonly expressed in human tissues, and it is the precursor protein of amyloid β (Aβ) peptides. Studies have shown that the abnormal expression of APP is harmful,[12–16] as such, developing targeting tools to control APP expression is of great significance.

Major G4 targeting tools include the G4 chemicals,[17–19] such as pyridostatin, PhenDC3, and G4 antibody/nanobody[20–22] such as BG4 and SG4. They have been used to detect G4 formation and control G4-linked functions both in vitro and in cells.[1,8,17–22] While they have strong binding preference to G4 motifs over non-G4s, they are generally not sufficiently selective to distinguish between different G4s,[1,8,17–22] raising an overarching question in the community that whether novel G4-targeting tools can be developed for precise G4 targeting.[23] Aptamers are short single-stranded DNA or RNA oligonucleotides that fold into unique structure scaffolds and bind to the target of interest, including proteins, cells, small molecules, and nucleic acid structures.[24–26] L-Aptamers are composed of L-RNA (enantiomeric form of naturally occurring D-RNA) that is unnatural, so they cannot be recognized by nucleases and cannot trigger immunogenicity, which

H. L. Lau, H. Zhao, H. Feng, C. K. Kwok
Department of Chemistry and State Key Laboratory of Marine Pollution
City University of Hong Kong
Kowloon Tong, Hong Kong, SAR, China
E-mail: ckkwok42@cityu.edu.hk

C. K. Kwok
Shenzhen Research Institute
City University of Hong Kong
Shenzhen 518057, China

The ORCID identification number(s) for the author(s) of this article can be found under https://doi.org/10.1002/smtd.202401097

DOI: 10.1002/smtd.202401097

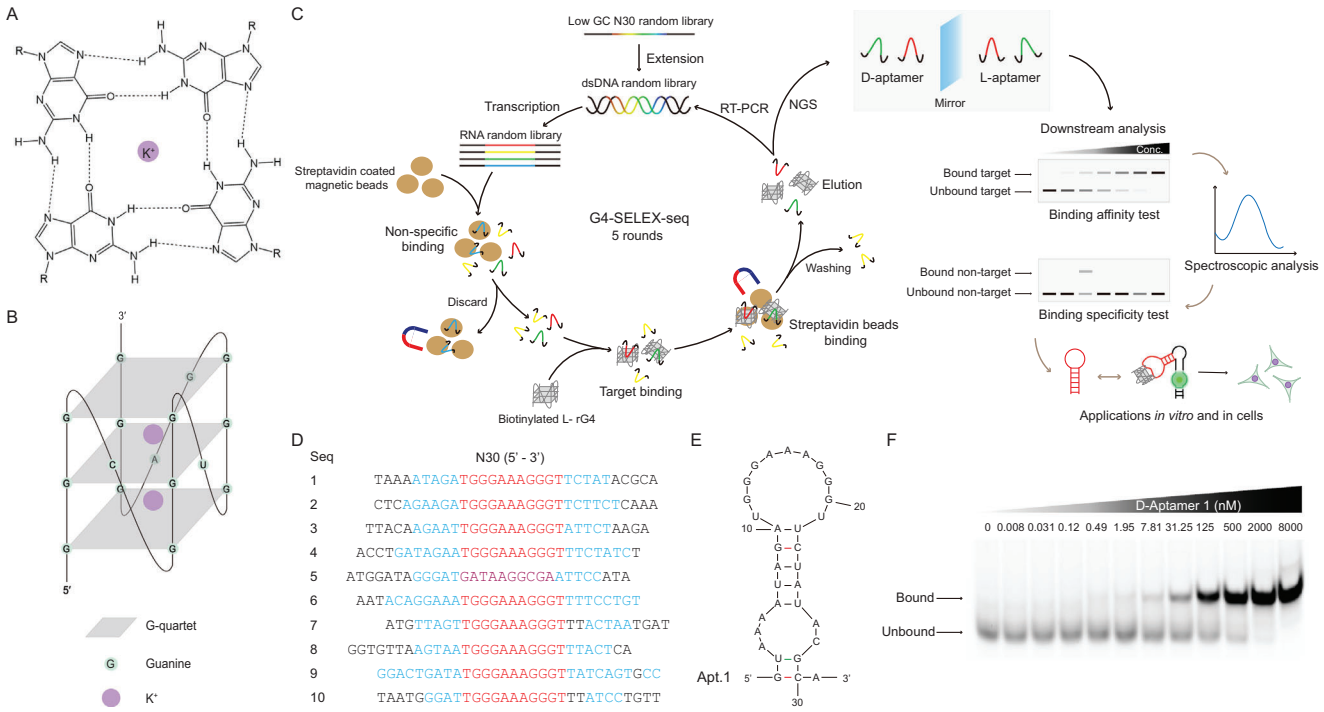

Figure 1. G4-SELEX-seq with a low GC N30 random library enables the identification of novel non-G4-containing RNA aptamers that bind to *APP* L-rG4. A) Chemical structure of the G-quartet and B) *APP* 3'UTR RNA G-quadruplex. C) Scheme of G4-SELEX-seq and downstream analysis on the aptamer candidates. D) NGS results after five rounds of G4-SELEX-seq. The top 10 candidates are shown. The red and purple color indicates the conserved and non-conserved regions observed among most candidates, respectively. Blue and black colors indicate the base pair and single-stranded region in each candidate, respectively. E) Mfold predicted RNA secondary structure of Apt.1. Apt.1 is 31 nucleotides long in length, with a hairpin loop structure, and contains an internal loop on the stem region. An extra G base at the 5' end of Apt.1 is added for T7 in vitro transcription of RNA for binding analysis. The resulting extra GC base pair can strengthen the stem structure and improve the structural stability of Apt.1. F) The binding between D-Apt.1 and FAM *APP* L-rG4 target via EMSA. With increasing concentrations of D-Apt.1, the fluorescent signals of the FAM *APP* L-rG4 target shift upward, indicating the interaction between D-Apt.1 and FAM *APP* L-rG4. Values were obtained from three replicates and error bars display the standard error of the mean.

greatly enhances their biostability in biological media.[27–29] They are usually developed using in vitro selection, and systematic evolution of ligands by exponential enrichment (SELEX).[24–26,30] Recently, we have developed a robust SELEX platform (rG4-SELEX) to generate L-RNA aptamers that target rG4,[23] and showcased that these aptamers can recognize its target and control gene regulation in cells by targeting rG4 of interest.[31–33] However, their binding specificity is non-ideal due to their off-target binding to other similar rG4s.[32,33] From our detailed sequence and structural analysis, we found that these L-RNA aptamers all contain the rG4 motif itself, which may potentially lead to this insufficient binding specificity toward the rG4 target and closely related rG4 motifs. Until now, no non-G4-containing L-RNA aptamer was developed to target G4 structures. Herein, we hypothesize that the absence of an rG4 motif in L-RNA aptamer can improve its binding specificity to the rG4 target of interest.

Fluorogenic RNAs are RNA molecules that bind and activate the fluorescence of its corresponding fluorophore.[34–37] The first fluorogenic aptamer developed is the Spinach aptamer which activates the HBI ligands fluorescence.[38] Next, several fluorogenic aptamers were developed including Mango,[39] Broccoli,[40] Corn,[41] Chili,[42] and etc. The pepper aptamer is one of the fluorogenic RNAs developed that activates HBC ligands of a broad spectral range from cyan to red.[43] Recently, the secondary and tertiary structure of the pepper–HBC complex was reported, revealing that the pepper aptamer binds HBC ligands without interaction with the P1 and P3 stem.[44,45] Over recent years, the pepper aptamer was developed as bi-functional fluorescent light-up aptamers (FLAPs) by fusing with target-binding aptamers at P1 or P3 stem, to detect small molecules or proteins in the presence of HBC ligands.[46–48] While these pepper-based detections were based on genetically encoded D-pepper aptamer, we hypothesize that the L-pepper-HBC system is also feasible, as the HBC ligands are achiral. Till now, pepper-based rG4 detection has not been investigated, by fusing L-Aptamer that targets rG4 structure with L-pepper, we hypothesize that a L-RNA-based fluorogenic bi-functional aptamer can be developed, which will further broaden the application of fluorogenic RNAs. In this study, we couple the low GC content template library with our SELEX platform (G4-SELEX-seq) (Figure 1C), and develop a novel L-RNA aptamer, L-Apt.1-1, to recognize *APP* rG4 structure. We show that our newly developed L-Apt.1-1 is a non-G4-containing aptamer and has superior binding specificity compared with the prior art (i.e., G4-containing L-Apt.8f), and it can suppress APP expression via targeting the rG4 motif in cells. Furthermore, L-Apt.1-1 can be connected to the L-pepper aptamer to generate a bi-functional FLAP for in vitro detection and cellular imaging of *APP* rG4 in the presence of HBC530.

2. Results

2.1. Identification of a Novel Non-rG4-Containing D-RNA Aptamer That Binds *APP* L-rG4

In G4-SELEX-seq, the G4-SELEX part involved stereospecific enzymes that could only recognize D-form nucleic acids, thus the chirality of the library pool and *APP* rG4 target was reversed to begin the first selection cycle with a D-library pool and biotin-*APP* L-rG4 target (Figure 1C). In order to increase the probability of successfully obtaining non-G4-containing aptamer candidates, we have introduced a low GC-content library pool to minimize the enrichment of G-rich sequences that may promote G4 formation in the initial G4-SELEX round. The library pool was designed with randomized low GC 30 nt region, flanked by primer binding sequences at 5' and 3' ends with T7 promoter sequence included (Table S1, Supporting Information). The DNA library was transcribed to the RNA library for selection. Through the SELEX cycles, non-target binding sequences were discarded, while the biotinylated target-aptamer complexes were pulled down by tRNA-blocked streptavidin-coated magnetic beads. The target-binding aptamer candidates were then eluted and reverse-transcribed for PCR amplification (Figure 1C). To select stronger binding aptamer candidates, the SELEX cycles were then repeated with increasing stringency of selection conditions in subsequent rounds (Table S2, Supporting Information). After five rounds of selection, the aptamer candidates were sequenced by next-generation sequencing (NGS) (Tables S3–S7, Supporting Information).

From the NGS results, a low GC ratio (≈30%) was observed in the original random sequences of the N30 library (Table S3, Supporting Information). During the SELEX process, enrichment of specific sequences was observed, for example, aptamer candidate 1 in round 5 from Table S7 (Supporting Information) increased from 0.00015% of reads (ranked 92 928) in round 2 to 0.00538% (ranked 32) in round 3, 0.04737% (ranked 6) in round 4, and 0.20879% (ranked 1) in round 5 (Tables S4–S7, Supporting Information). With close inspection of the sequence data, we observed that there was an enriched conserved region 5'-TGGGAAAGGGT-3' among the aptamer candidates in the NGS result (Red sequences in Figure 1D, and bold sequences in Tables S3–S7, Supporting Information). To shortlist candidates for downstream experiments, we first used the Mfold program[49] to predict the secondary structures of aptamer candidates with or without linker regions (Figure S1, Supporting Information). It is worth noting that Mfold cannot predict G4 structure formation, so we also performed G4 prediction analysis using G4RNAscreener v.0.3.[50] The G4 prediction scores indicated that most aptamer candidates are unfavorable for forming G4 structures (Table S3–S7, Supporting Information). Considering the sequence enrichment and percentage of reads (Tables S3–S7, Supporting Information), consistency of the secondary structures with or without linkers (Figures S1, Supporting Information), and the low G4 prediction scores (Table S7, Supporting Information), we shortlisted Apt.1, 2, 4, 6, 9, and 13 (Table S7, Supporting Information) for an initial binding test by electrophoretic mobility shift assay (EMSA). Our results showed that Apt.1, 2, 4, 6, and 9 have strong binding with 5' FAM *APP* L-rG4 target compared with Apt.13 (Figure S2, Supporting Information). Based on these binding results, we selected Apt.1 for downstream analysis as it is also most enriched in the final round (ranked 1) (Table S7, Supporting Information).

The Mfold predicted RNA secondary structure of Apt.1 is shown in Figure 1E. An extra 5' G was appended for in vitro RNA transcription purposes. We first performed EMSA full-range binding test for D-Apt.1 against FAM *APP* L-rG4, the results showed that with increasing concentrations of D-Apt.1, the fluorescent signals emitted from unbound FAM *APP* L-rG4 target shift upward, indicating the interaction between D-Apt.1 and FAM *APP* L-rG4 and thus the slower migrating band on the gel (bound) (Figure S3, Supporting Information). The K_d was determined to be 66.87 ± 7.07 nM for the T7 in vitro transcribed RNA oligonucleotide (Figure S3, Supporting Information), and was similar to the binding affinity using a chemically synthesized RNA oligonucleotide, with a K_d value of 42.28 ± 4.48 nM (Figure 1F). To summarize, we have identified novel non-G4-containng aptamers targeting *APP* rG4 with low GC N30 library input and NGS readout, and we found that D-Apt.1 was able to bind *APP* L-rG4 target with nanomolar binding affinity.

2.2. Spectroscopic and Mutagenesis Analysis Reveals the Non-rG4-Containing Structure of D-Apt.1-1 and the Key Nucleotides for Target Recognition

To improve the binding affinity of D-Apt.1 to *APP* L-rG4 target, we strengthened its stem by replacing the internal loop with GC base pair to stabilize the hairpin loop structure, referred to as D-Apt.1-1 shown in **Figure 2A**. We speculated that by enhancing the structural stability of D-Apt.1-1 in the stem region, D-Apt.1-1 can bind stronger to *APP* L-rG4. We then performed EMSA full-range binding and found that D-Apt.1-1 had improved binding affinity to *APP* L-rG4, with a dissociation constant (K_d) of 16.98 ± 3.29 nM (Figure 2B,C), compared to D-Apt.1 of 42.28 ± 4.48 nM.

The G4 prediction result mentioned above for D-Apt.1 (Table S6, Supporting Information) and D-Apt.1-1 (Figure S4A, Supporting Information) suggested them to have a low probability of forming G4, however, it is always good practice to also perform experimental validation.[1] In addition, these G4 prediction tools cannot identify non-canonical G4s and inter-molecular G4s well due to their limited training sets.[51,52] Next, we performed multiple spectroscopic analyses for G4 detection purposes[1] to see if D-Apt.1-1 would form a G4 structure or not. Using circular dichroism, our results showed no significant enhancement peaks at 240 and 260 nm in the case of K^+ compared to Li^+ conditions, indicating no G4 structure forming in D-Apt.1-1 (Figure S4B, Supporting Information). To further support the findings, we performed ligand-enhanced fluorescence assay using G4-specific ligands, including NMM and ThT. The results showed the ligand fluorescence is independent of K^+ and Li^+ conditions in the presence of D-Apt.1-1, suggesting no rG4 formation in D-Apt.1-1 (Figure S4C,D, Supporting Information). Next, we tested whether D-Apt.1-1 forms an intermolecular rG4 structure upon binding to *APP* L-rG4 target. We performed a binding test for D-Apt.1-1 and FAM *APP* L-rG4, with D-Apt.8f (33 nt), a published aptamer that we found to form intramolecular rG4,[33] that also

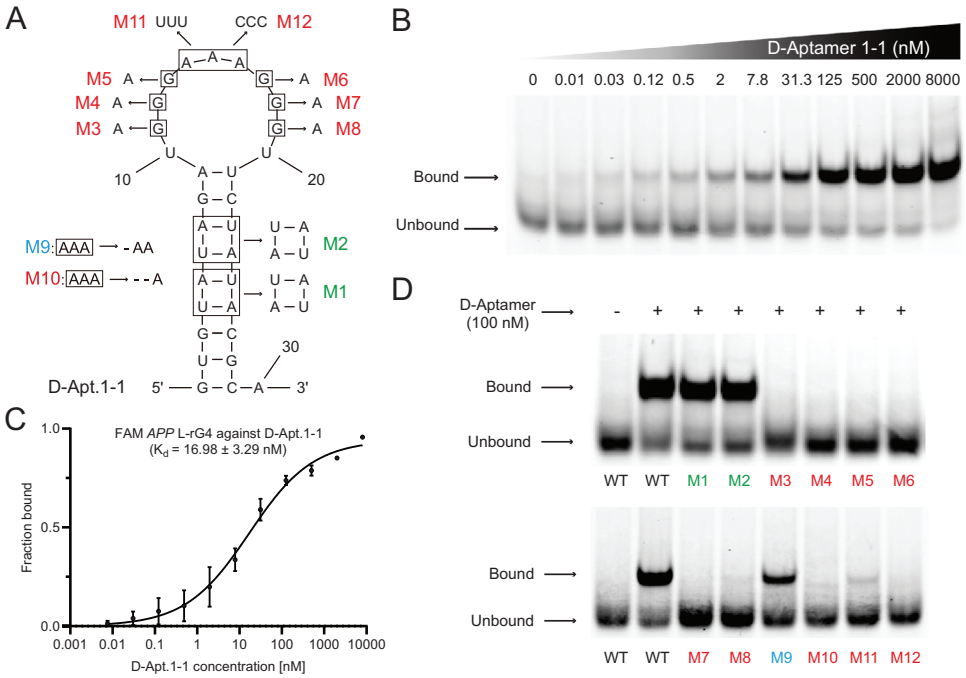

Figure 2. Characterization of Apt.1-1 shows strong binding affinity to FAM *APP* L-rG4 target and reveals key nucleotides for target recognition. A) Mfold predicted RNA secondary structure of Apt.1-1. Apt.1-1 is generated from Apt.1 by replacing the internal loop with a strong GC base pair. Twelve mutants of Apt.1-1 were designed (M1–M12). B) The binding between D-Apt.1-1 and FAM *APP* L-rG4 target using EMSA. With increasing concentrations of D-Apt.1-1, the fluorescent signals of FAM *APP* L-rG4 target shifted upwards, indicating the interaction between D-Apt.1-1 and FAM *APP* L-rG4. C) The binding curve of D-Apt.1-1 to FAM *APP* L-rG4 obtained from EMSA result in (B), and the dissociation constant (K_d) was determined to be 16.98 ± 3.29 nM. D) The binding of D-Apt.1-1 wildtype and mutants to FAM *APP* L-rG4 target via EMSA. Base-pair co-variation mutants (M1 and M2) resulted in no reduction in binding ability. Mutations on the Gs on the loop of D-Apt.1-1 abolished the binding (M3–M8). The deletion of one A on the loop weakened the binding (M9), and the deletion of two As completely disrupted the binding (M10). Mutation of AAA on the loop to UUU (M11) and CCC (M12) strongly disrupted the binding. Green, blue, and red colors indicate the no change, small change, and strong change in binding of the mutant constructs, respectively, and the symbol "-" indicates the deleted nucleotides. Values were obtained from three replicates and error bars display standard error of mean.

targets *APP* L-rG4 structure as control. The results showed that D-Apt.1-1-FAM *APP* L-rG4 complex migrated slightly faster than D-Apt.8f-FAM *APP* L-rG4 complex, which indicates the smaller size of D-Apt.1-1 (30 nt) comparing with D-Apt.8f. Also, no upper band was observed above the D-Apt.1-1-FAM *APP* L-rG4 complex band, eliminating the probability of intermolecular rG4 formation of D-Apt.1-1 upon binding to *APP* L-rG4 structure (Figure S5, Supporting Information). After that, we tested whether D-Apt.1-1 is capable of unwinding FAM *APP* L-rG4 to form an alternative hybrid G4 structure between aptamer and target. We performed a binding test by refolding D-Apt.1-1 and FAM *APP* L-rG4 together in one sample solution using slow cooling from 95 °C to 4 °C, to enhance their hybrid G4 formation as well as the binding affinity (Figure S6A, Supporting Information). The K_d generated was 7.24 ± 0.82 nM, which was similar to the original reported refolding method (16.98 ± 3.29 nM), indicating no hybrid G4 structure was formed between D-Apt.1-1 and FAM *APP* L-rG4 target (Figure S6B, Supporting Information). These findings validate the G4 prediction result and indicate that D-Apt.1-1 does not contain any G4 motif in the aptamer structure either in the presence or absence of *APP* L-rG4 target.

The Mfold program predicted the RNA secondary structure of D-Apt.1-1 as a hairpin structure (Figure 2A). We hypothesized that the conserved sequence on the loop (Figure 1D), i.e., UGGGAGGGU, is essential for its binding to *APP* L-rG4 due to its high occurrence in NGS sequencing data (Tables S3–S6, Supporting Information), and the base pair co-variation we observed in the stem region, as well as variation in stem length (Figure 1D), implied that the stem structure is likely important for the binding. To investigate the interaction between D-Apt.1-1 and *APP* L-rG4, we performed mutagenesis analysis on D-Apt.1-1. We designed 12 mutated constructs of D-Apt.1-1 to evaluate the effect of sequence and structure towards *APP* L-rG4 target binding using EMSA (Figure 2A). We first designed two mutants (M1 and M2) that flipped two of the base pairs in the stem region. The results showed these co-variation mutants had similar binding to wildtype, suggesting the base pair structure rather than the sequence in the stem was important for binding, validating the base pair covariation data observed from the NGS (Figure 1D and Table S6, Supporting Information). Next, we mutated the Gs on the loop to As (M3–M8) to verify whether the bases on the loop were essential for binding, and the binding was disrupted in all constructs (Figure 2D). Then, we deleted the As on the loop, the results show that deleting one A base could weaken the binding (M9), and deleting two A bases completely disrupted the binding (M10), indicating that the binding is sensitive to the number of A bases (Figure 2D). Lastly, we

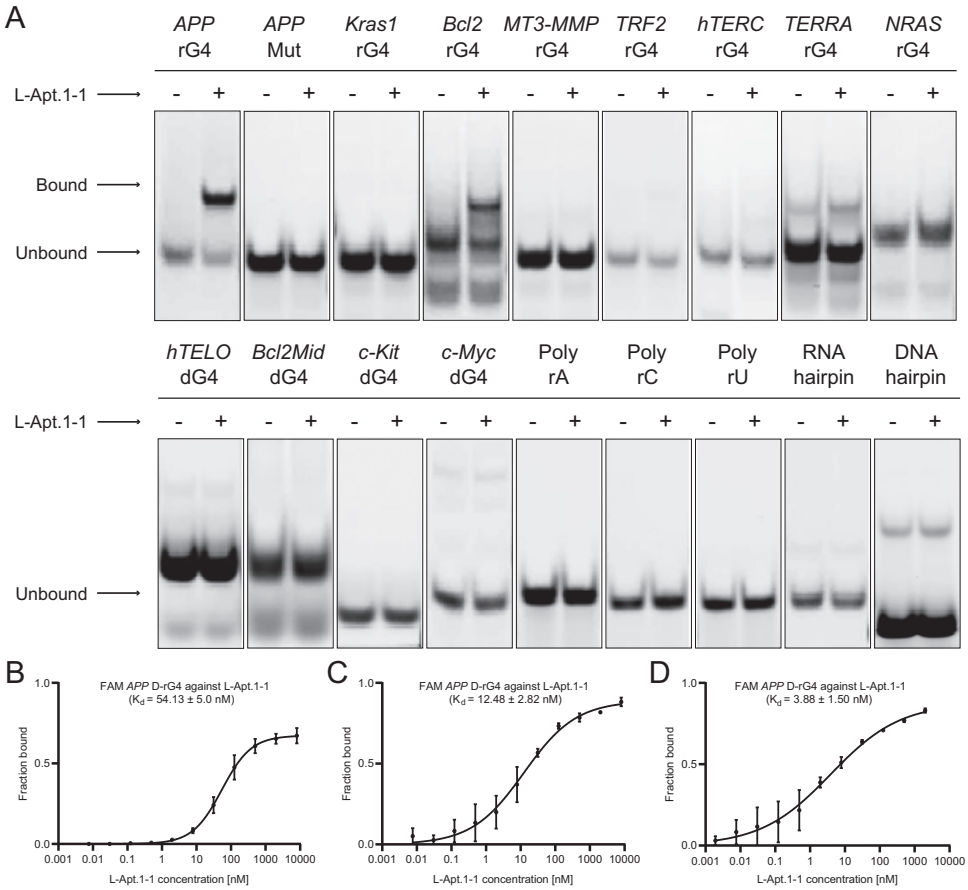

Figure 3. Binding specificity analysis and magnesium ion dependence of L-Apt.1-1–*APP* D-rG4 interaction. A) L-Apt.1-1 showed high binding specificity to FAM *APP* D-rG4. The binding specificity of L-Apt.1-1 was tested with 18 constructs, including several rG4s, dG4s, RNA/DNA hairpins, single-stranded RNAs, and *APP* rG4 mutant, with its intended target *APP* rG4 as control. Except for binding weakly to *Bcl2* rG4, no binding was observed for the remaining 16 unintended targets, indicating the high specificity of L-Apt.1-1 to the intended target *APP* rG4. B) The binding curve of L-Apt.1-1 to FAM *APP* D-rG4 target in 0 mM $MgCl_2$, the dissociation constant (K_d) was determined to be 54.13 ± 5.0 nM. C) The binding curve of L-Apt.1-1 to FAM *APP* D-rG4 target in 1 mM $MgCl_2$, the dissociation constant (K_d) was determined to be 12.48 ± 2.82 nM. D) The binding curve of L-Apt.1-1 to FAM *APP* D-rG4 target in 2 mM $MgCl_2$, the dissociation constant (K_d) was determined to be 3.88 ± 1.50 nM. Values were obtained from three replicates and error bars display the standard error of mean.

mutated the AAA on the loop to UUU (M11) and CCC (M12), and weak binding was observed in M11 and no binding was observed in M12, illustrating that the AAA sequence was important for binding (Figure 2D). Overall, we demonstrated experimentally that D-Apt.1-1 indeed does not contain G4 motif, and its sequence on the loop region is critical for target recognition, and the stem region holds the aptamer structure into a hairpin structure.

2.3. L-Apt.1-1 Specifically Recognizes D-*APP* rG4 Over Non-Targets, and the Interaction is Magnesium Ion Dependent

Next, we investigated the binding specificity of L-Apt.1-1 by testing its binding with 18 constructs via EMSA, including several rG4s (*Kras1, Bcl2, MT3-MMP, TRF2, hTERC, TERRA, NRAS*), dG4s (*hTELO, Bcl2Mid, c-Kit, c-Myc*), RNA/DNA hairpins, single-stranded RNAs (poly rA/rC/rU), *APP* rG4 and *APP* rG4 mutant. No binding was observed for any of the dG4s, RNA/DNA hairpins, and single-stranded RNAs, indicating the high specificity of L-Apt.1-1 (**Figure 3A**). Given that *APP* rG4 (intended target) and other rG4s may share quite similar structural features, it is generally difficult to develop L-RNA aptamer that targets a specific rG4 motif.[23,32,33] Our previous attempt using L-Apt.8f to target *APP* D-rG4 was not entirely successful, as it was found to bind strongly to two of the unintended targets, *Bcl2* rG4 and *Kras1* rG4.[33] We hypothesized that non-G4-containing L-Apt.1-1 would perform better in the binding specificity test. Therefore, we tested the binding of L-Apt.1-1 to eight rG4 constructs to evaluate its binding specificity among the rG4 structures. The results showed that the binding of L-Apt.1-1 is specific to *APP* rG4, except that it only binds weakly to one of the rG4 non-targets (*Bcl2*) (Figure 3A). We further compared the binding of L-Apt.1-1 to *APP* D-rG4 and *Bcl2* D-rG4 by performing a full-range EMSA. The results showed that L-Apt.1-1 binds ≈20-fold stronger to *APP* D-rG4 than *Bcl2* D-rG4, with a dissociation constant (K_d) of 12.48 ± 2.82 nM and 266.0 ± 27.2 nM, respectively (Figure S7, Supporting Information). We also performed full binding for the *Kras1* rG4, and in

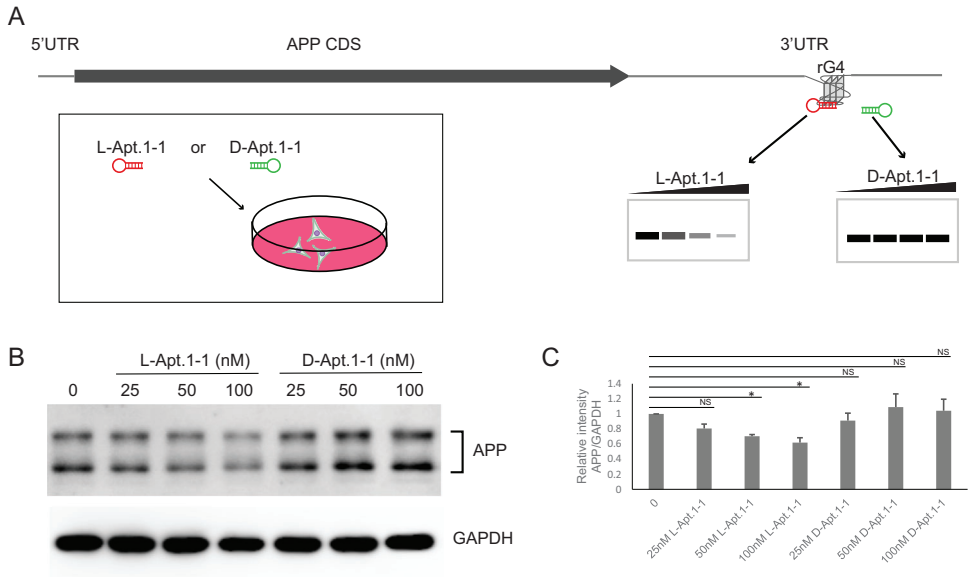

Figure 4. The effect of L-Apt.1-1 on the endogenous APP level in cells. A) Scheme of cell treatments. The rG4 is located at the 3'UTR of the *APP* mRNA. HeLa cells were transfected with different concentrations of L-Apt.1-1 or D-Apt.1-1 (0–100 nM), followed by western blot assay. B) Western blot analysis of endogenous APP level treated with L-Apt.1-1 or D-Apt.1-1 (0–100 nM). GAPDH was used as a loading control. C) Quantification of endogenous APP protein level relative to GAPDH. Values were obtained from three replicates and error bars display standard error of mean. $*p < 0.05$, meaning statistical significance. NS, not significance.

agreement with Figure 3A, no observable binding was detected, and the K_d was too weak to be determined (Figure S7, Supporting Information). Remarkably, the specificity result for L-Apt.1-1 was in great contrast to the rG4-containing L-RNA aptamer L-Apt.8f, in which it recognized not only to *APP* rG4 (K_d 13.02 ± 1.42 nM), but also recognized *Bcl2* rG4 and *Kras1* rG4 strongly, with K_ds of, 39.57 ± 8.25 nM and 71.74 ± 17.10 nM, respectively, under the same reaction conditions (Figure S8, Supporting Information). From the binding specificity results, we provide substantial evidence that L-Apt.1-1 preferentially binds to the intended target *APP* rG4.

Next, the enantiomeric specificity of Apt.1-1 was also tested, and the results showed that Apt.1-1 was enantiomeric-specific and could only bind to the target in its mirror form, i.e. *APP* D-rG4–L-Apt.1-1, or *APP* L-rG4–D-Apt.1-1, but not *APP* D-rG4–D-Apt.1-1 or *APP* L-rG4–L-Apt.1-1 (Figure S9, Supporting Information). This result is also consistent with previous studies on other aptamer–target pairs.[31–33] Next, we investigated the magnesium ion dependence of the binding of L-Apt.1-1 to *APP* D-rG4 under 0, 1, and 2 mM $MgCl_2$ using EMSA (Figure S10, Supporting Information). The K_{ds} were determined to be 54.13 ± 5.0, 12.48 ± 2.82, and 3.88 ± 1.50 nM, respectively, suggesting that magnesium ions can enhance the binding between L-Apt.1-1 and *APP* D-rG4 (Figure 3B–D). In addition, we investigated the potassium ion dependence of the binding of L-Apt.1-1 to *APP* D-rG4 under 0, 50, 100, and 200 mM potassium ions using EMSA (Figure S11A–D, Supporting Information). The K_{ds} were determined to be 387.11 ± 25.33, 28.72 ± 3.74, 13.11 ± 1.32, and 3.75 ± 0.31 nM, respectively (Figure S11F, Supporting Information). We speculated that this potassium ion dependency was mostly due to the destabilization of the *APP* rG4 with lower potassium ion concentrations (less thermostable), rather than to the aptamer-target recognition. To support this, we performed the binding test in 150 mM sodium ion condition (Figure S11E, Supporting Information), and the K_d was determined to be 35.41 ± 1.48 nM (Figure S11G, Supporting Information), which is comparable with the K_d generated in 50 mM potassium ion condition. To summarize, L-Apt.1-1 is highly specific to APP D-rG4 over other non-targets, and its binding is magnesium ion-dependent and RNA chirality-dependent.

2.4. Application of L-Apt.1-1 to Regulate APP Expression in Cells

To test whether L-Apt.1-1 can regulate endogenous APP protein expression by the interaction with the *APP* 3'UTR rG4 structure, we transfected cells with different concentrations of L-Apt.1-1 (0, 25, 50, and 100 nM), and detected the endogenous APP level by western blot (**Figure 4A**). We also transfected D-Apt.1-1 as a negative control, as we showed that D-Apt.1-1 did not bind to the *APP* D-rG4 target (Figure S9, Supporting Information). The result showed that L-Apt.1-1 can inhibit endogenous APP expression in a concentration-dependent manner. Compared with the non-treated group (0 nM), the APP protein expression levels treated with different concentrations of L-Apt.1-1 (25, 50, and 100 nM) were reduced by ≈19%, 30%, and 38%, respectively (Figure 4B,C). Consistent with the in vitro binding assay, the enantiomer D-Apt.1-1 treated group also showed no significant effect on the APP expression level (Figure 4B,C), compared to the non-treated group (0 nM). To further assess whether the inhibition effect is due to the transcription or translation, we performed a quantitative reverse transcription-polymerase chain reaction (qRT-PCR) to detect the mRNA level of *APP*. The result showed that neither L-Apt.1-1 nor D-Apt.1-1 affected the mRNA

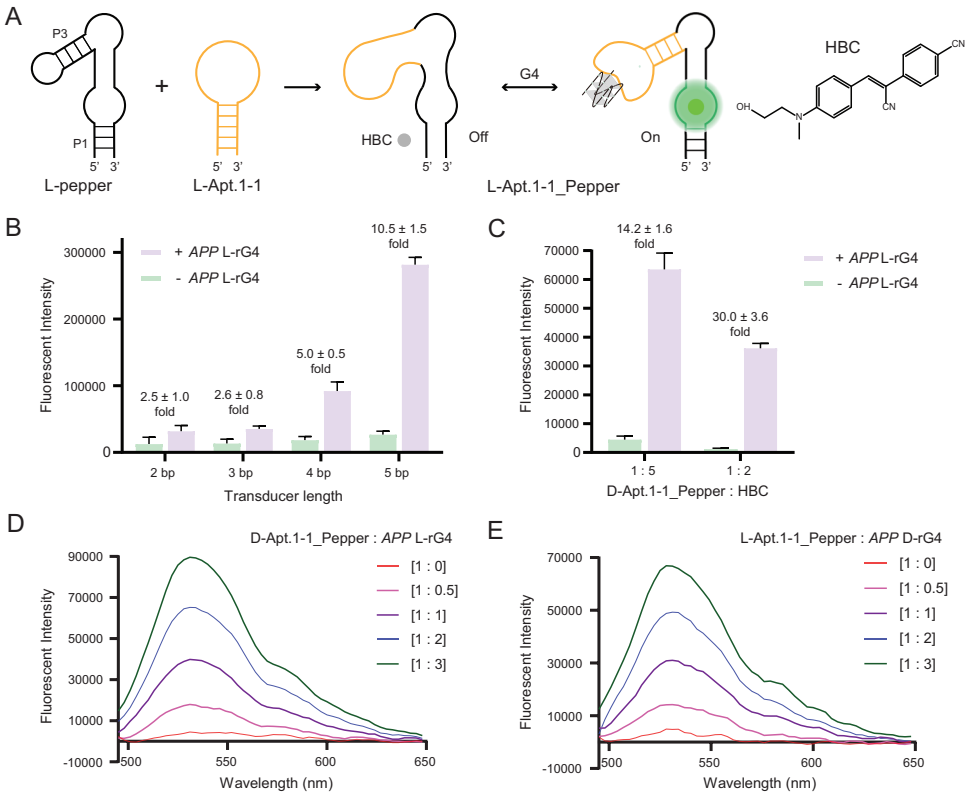

Figure 5. Design and optimization of the bi-functional FLAPs using Apt.1-1 and pepper aptamer against *APP* rG4 significantly enhanced HBC530 signal in vitro. A) Scheme of developing bi-functional FLAPs, P3_2bp, P3_3bp, P3_4bp, P3_5bp, and the structure of HBC ligand. B) Fold effects of bi-functional FLAPs with and without *APP* L-rG4 using different transducer lengths at P3 stem, P3_5bp generated best fold effect (D-Apt.1-1_Pepper). C) Fold effects of 0.5 μM of D-Apt.1-1_Pepper with different pepper:HBC ratio. D) Spectrum generated using D-Apt.1-1_Pepper against different concentrations of *APP* L-rG4, with the highest of 47.8 ± 3.7-fold. E) Spectrum generated using L-Apt.1-1_Pepper against different concentrations of *APP* D-rG4, with the highest of 44.5 ± 1.4-fold. Values were obtained from three replicates and error bars display standard error of mean.

level of *APP* (Figure S12, Supporting Information), indicating that the inhibition effect of L-Apt.1-1 is at the translation level but not at the transcriptional level. In addition, we tested the cytotoxicity of L-Apt.1-1 to HeLa cells. HeLa cells were treated with different concentrations of L-Apt.1-1 (25, 50, and 100 nM) for 48 h. There was no significant difference in cell survival rate between the L-Apt.1-1-treated group (25, 50, and 100 nM) and the control group (0 nM), indicating that L-Apt.1-1 was not toxic to HeLa cells, and the APP regulation was specific (Figure S13, Supporting Information). We also tested the stability of Apt.1-1 in biological environment with the treatment of 5% fetal bovine serum (FBS) or 10 ng μL^{-1} RNase A (Figure S14A, Supporting Information). Low degradation of L-Apt.1-1 (>90% retained) was observed in 2 h, while D-Apt.1-1 was all degraded at 120 min (Figure S14B,C, Supporting Information), indicating the enhanced biostability of L-oligonucleotides potential for biological applications. In this sense, we confirmed the binding of L-Apt.1-1 to FAM *APP* D-rG4 in HeLa cell lysate (Figure S15A, Supporting Information), the K_d was determined to be 30.11 ± 2.68 nM, which indicated L-Apt.1-1 maintained its binding activity in cellular conditions mimic (Figure S15B, Supporting Information). Taken together, L-Apt.1-1 is biostable, non-toxic, and can inhibit the translation of APP by targeting *APP* 3'UTR rG4 motif in cells.

2.5. Development of the Bi-Functional FLAP Using Apt.1-1 and Pepper Aptamer Allows *APP* rG4 Detection In Vitro and in Cells

Recently, the pepper aptamer was applied to the detection of small molecules and proteins.[46–48] However, pepper-based rG4 detection was not developed, and the L-pepper system was not investigated. Here, we applied L-Apt.1-1 as a pepper-based rG4 sensor to achieve specific fluorescence light-up against *APP* rG4, by designing a bi-functional FLAP that binds to both HBC530 ligand and *APP* rG4 in different motifs (**Figure 5**A and S16A, Supporting Information). We hypothesized that the HBC530 ligand could bind to L-pepper with similar affinity to D-Pepper as it was achiral (Figure 5A). First, we tested the system in D-form, and designed three bi-functional FLAPs with transducer lengths ranging from one to three base pairs at the P1 stem (P1_1bp, P1_2bp, P1_3bp) (Figure S16A and Table S1, Supporting Information). We tested the fluorescent light-up of HBC530 ligand in the presence of bi-functional FLAPs with or without *APP* L-rG4, and the results showed that all samples exhibited low fluorescent signal when *APP* L-rG4 was absent, and restored fluorescence when *APP* L-rG4 was present, with a best fold effect of 5.3 ± 1.9 (Figure S16B, Supporting Information). This indicated the bi-functional FLAPs could only regenerate the HBC binding pocket and enhance HBC fluorescence by binding to *APP* L-rG4 target that provides extra

stabilization. We then tested whether the fusion of Apt.1-1 to the P3 stem of pepper aptamer could improve the fold effect. We designed four bi-functional FLAPs with transducer lengths ranging from two to five base pairs (P3_2bp, P3_3bp, P3_4bp, P3_5bp) (Figure 5A and Table S1, Supporting Information), and the performance were improved, with a best fold effect of 10.5 ± 1.5 from P3_5bp (D-Apt.1-1_Pepper) (Figure 5B), fluorescent spectrum is shown in Figure S17 Supporting Information). To further improve its fold effect, we reduced the system concentration by half, using 0.5 µM of D-Apt.1-1_Pepper, and successfully improved the fold effect to 14.2 ± 1.6 fold (Figure 5C). We also investigated whether the concentration of HBC530 ligand affected the fluorescent signal by reducing the pepper:HBC ratio from 1:5 to 1:2, and the fold effect was improved to 30.0 ± 3.6 (Figure 5C). Then, we tested whether the fluorescent light-up of the D-Apt.1-1_Pepper system was dependent on the target concentrations. The results showed that the fluorescent signals were enhanced with increasing *APP* L-rG4 concentrations, with the highest fold of 47.8 ± 3.7, indicating that the system could be applied to detect targets in different concentrations (Figure 5D).

We next investigated the performance of L-Apt.1-1_Pepper, the results showed that L-Apt.1-1_Pepper could respond to different *APP* D-rG4 concentrations in the presence of HBC530 ligand, with the highest fold of 44.5 ± 1.4, which supported our hypothesis (Figure 5E). As provided in the original study on the magnesium ions dependency of the pepper-HBC interaction[43] and the magnesium ions dependency of L-Apt.1-1-*APP* D-rG4 interaction done by us, we investigated the influence of magnesium ions concentrations on L-Apt.1-1_Pepper system. The results showed that under 0 mM magnesium ion, no fluorescent light-up could be observed, while the fluorescent signal increased in 5 mM magnesium ions, indicating that the system was magnesium ion dependent (Figure S18, Supporting Information). Given that L-Apt.1-1 had a high specificity to *APP* D-rG4 as shown in Figure 3A, we performed a specificity test on L-Apt.1-1_Pepper against *APP* D-rG4, and other non-targets including DNA hairpin, dG4, rG4, and *APP* L-rG4. Enhanced fluorescent signal could be observed in the presence of *APP* D-rG4, but not in other non-targets, indicating that the L-Apt.1-1_Pepper system can achieve specifically fluorescent light-up of its intended target (Figure S19, Supporting Information). To summarize, L-Apt.1-1_Pepper can specifically detect *APP* D-rG4 in a concentration-dependent manner in vitro, which motivated us to perform cellular imaging of *APP* D-rG4 using L-Apt.1-1_Pepper.

The in vitro success light-up of L-Apt.1-1_Pepper by the *APP* rG4 encouraged us to apply it to cells. Due to the low abundance of endogenous mRNA, it is hard to detect rG4 directly. Thus, we transfected cells with TAMRA-labeled *APP* rG4 motif RNA for detection. To show the light-up fluorescence is rG4 structure dependent, we also designed a rG4 mutant group (mut) as control by the mutation of middle G of the G tracts to A to disrupt G4 structure. After transfection, cells were stained with L-Apt.1-1_Pepper in the presence of HBC530 and scanned by confocal microscopy (**Figure 6A**). As shown in Figure 6B,C, both wt and mut groups showed red TAMRA foci, indicating the successful transfection of wt/mut *APP* rG4 oligos into HeLa cells. For wt group, L-Apt.1-1_Pepper foci were observed, and the L-Apt.1-1_Pepper foci colocalized well with the TAMRA signal at the ratio of ≈72%, indicating that L-Apt.1-1_Pepper recognized *APP* rG4 in cells and was light-up upon binding to *APP* rG4 in the presence of HBC530. For mut group, however, there was almost no L-Apt.1-1_Pepper signal at all, with a co-localization ratio of ≈3%, indicating the recognition and light-up mode was rG4 structure dependent (Figure 6B,C). Besides, we also tried to apply L-Apt.1-1_Pepper in another cell line, HEK 293T cell. As shown in Figure S20 (Supporting Information), the confocal imaging showed a similar result that L-Apt.1-1_Pepper can light-up well only in wt group (≈67% co-localization ratio), while not in mut group (≈2% co-localization ratio), further confirming the general use of the probe. Overall, L-Apt.1-1_Pepper can be used to visualize the specific *APP* rG4 structure in cells as a light-up probe.

3. Discussion

In this work, we employed a low GC content library template in G4-SELEX-seq, and subsequently generated L-Apt.1-1 (30 nt), which to the best of our knowledge is the first non-rG4 containing L-RNA aptamer developed to recognize any rG4 target and regulate gene expression in cells. We also engineered the L-Apt.1-1 with L-pepper to generate the first L-RNA-based bifunctional fluorescent aptamer system for G4 detection and imaging. In the following, we will discuss insights gathered from our data, compare with the results from our previous works, and offer suggestions for further development of L-RNA aptamers for selective G4 targeting, imaging, and diverse G4-related applications.

Given that our previously developed rG4-targeting L-RNA aptamers contain rG4 motif,[31–33] one of the key questions we and the associated research communities raised was whether rG4 motif is always necessary for the interaction, and whether non-G4 containing L-RNA aptamer can ever be developed, and if so, how similar or difference will the binding affinity and specificity be between the two types of L-RNA aptamers. From our results in this work, we realized that the successful generation of the first non-rG4 containing L-Aptamer, i.e, L-Apt.1-1, is largely facilitated by the use of low GC content library template, as we used the normal GC content library template before for the same target and was only able to obtain an rG4-containing L-RNA aptamer (L-Apt.8f).[33] We also think that the use of NGS as the readout in G4-SELEX-seq increases the throughput and chance for us to capture more non-G4-containing aptamer candidates, as well as the ability to follow the aptamer candidate evolution in each SELEX round to identify key sequence and structure features of aptamer candidates, as compared to the limited cases when using Sanger sequencing as readout.[23,31–33] For example, we have observed clear enrichment of the candidates with the TGGGAAAGGGT sequence motif in later SELEX rounds (Figure 1D and Tables S3–S7, Supporting Information), and our mutagenesis data showed that the conserved sequence motif formed the loop region of the aptamer and most of the nucleotides are critical for target recognition (Figure 2A,D).

For Apt.1-1, we have carried out spectroscopic assays such as CD and G4-ligand enhanced fluorescence assays to verify that the aptamer does not possess any distinct G4 spectroscopic features (Figure S4, Supporting Information). We also verified that Apt.1-1 does not form intermolecular G4 or hybrid G4 with *APP* rG4 via gel analysis (Figures S5 and S6, Supporting Information). In addition, our earlier study reported that *APP* rG4 is thermostable with a Tm of > 95 °C under 150 mM K^+ ion condition.[11]

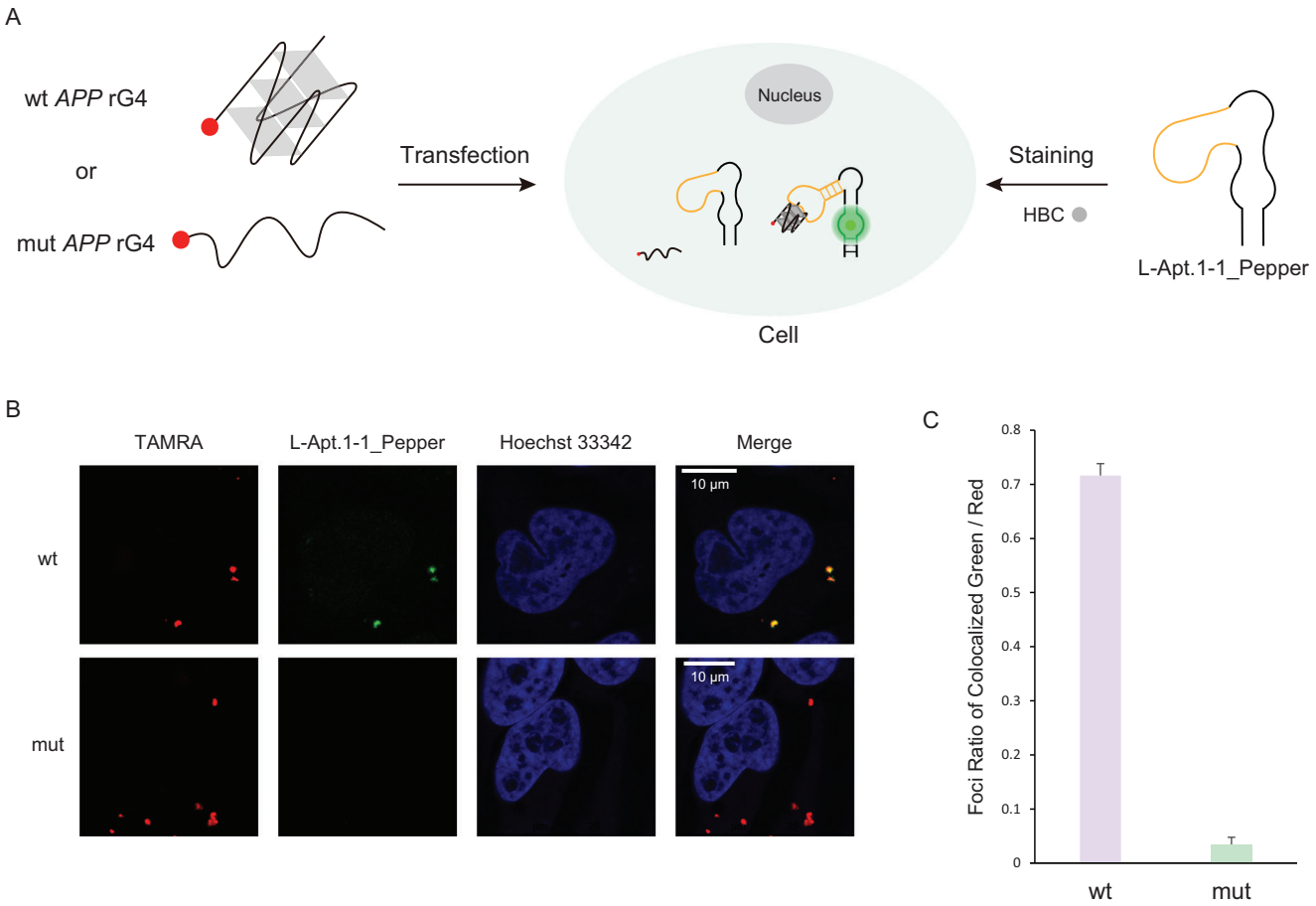

Figure 6. Light-up of *APP* rG4 motif using L-Apt.1-1_Pepper and HBC530 in HeLa cells. A) Scheme of cell imaging process. B) Confocal imaging of TAMRA-labeled wt/mut *APP* rG4 motif treated with L-Apt.1-1_Pepper and HBC530. Hoechst 33342 is to stain the nucleus. The scale bar is shown in a white line. C) Quantification of the overlap ratio of L-Apt.1-1_Pepper foci and *APP* rG4 foci (red) for wt and mut groups. About 750 foci for wt group and 1000 foci for mut group were counted. Values were obtained from three replicates and error bars display standard error of mean.

Therefore, it is unlikely that the aptamer can open the *APP* rG4 structure to form a new hybrid G4 structure. The binding affinity of L-Apt.1-1 and L-Apt.8f are similar, with K_d values of 12.48 ± 2.82 nM and 13.02 ± 1.42 nM, respectively, toward *APP* rG4 target (Figure 3C and Figure S8, Supporting Information). Notably, we observed that L-Apt.1-1 was able to achieve much better binding specificity towards *APP* rG4 target compared to the L-Apt.8f. From the results, we found that L-Apt.1-1 did not interact with off-target *Kras1* rG4 (K_d too weak to be determined) and much weaker to *Bcl2* rG4 (K_d 266.0 ± 27.2 nM) (Figure S7, Supporting Information), with a difference of ≈20-fold in K_d values. This is in stark comparison to L-Apt.8f that binds to *Kras1* rG4 and *Bcl2* rG4 with K_d values of 71.74 ± 17.10 nM and 39.57 ± 8.25 nM, respectively (Figure S8, Supporting Information), supporting that non-rG4 containing L-RNA aptamer can improve binding specificity while maintaining binding affinity to rG4 target of interest. Future high-resolution 3D structures will facilitate us to understand the structural basis of the aptamer and aptamer-target interaction, and provide us more insights for the refinement of the aptamer sequence and structure for even more specific rG4 targeting.

L-Aptamers are composed of unnatural nucleic acids, which are biostable in complex biological media for different biological applications in cells. We have tested and verified this case with FBS and ribonuclease A in this work and showed that the L-form aptamer (L-Apt.1-1) was resistant to ribonuclease degradation for hours, while the D-form aptamer (D-Apt.1-1) was degraded within 30 min (Figure S14, Supporting Information). Importantly, L-Apt.1-1 can be transfected into cells to regulate gene expression at the translational level by targeting the rG4 of interest without observable cytotoxicity. Further use of L-Apt.1-1 in other G4-mediated biological applications will allow us to understand gene regulation and cellular processes related to APP, which may play an important role in the prevention and treatment of Alzheimer's diseases in the future. Moreover, while most current G4 targeting tools, such as G4 ligands and G4 antibodies/nanobodies, have high specificity for G4 over non-G4s, they have limited specificity between G4s, limiting their applications such as precise gene control via targeting of specific G4 of interest.[23] The promising ability of L-RNA aptamer, especially for the non-G4-cotaining one reported here, to target G4 structure of interest can be further refined, and the aptamer selection approach may be expanded to

recognize other canonical and non-canonical nucleic acid structures.

The pepper D-RNA aptamer has been applied to image target molecules such as small molecules and proteins in a genetically encoded manner.[46–48,53] In this work, we developed the first L-RNA-based fluorogenic bi-functional aptamer to light up rG4 of interest in vitro and in cells. Using the highly specific L-Apt.1-1_Pepper, we have reported the first nucleic acid-based cellular imaging of a particular rG4 structure (Figure 6). Notably, L-pepper aptamer takes the advantage of high stability of L-oligonucleotides in cellular environment, which is likely to produce a more stable fluorescent signal. Further investigation on the L-pepper aptamer and its achiral HBC ligand for generating bi-functional FLAPs will likely broaden the application of the pepper aptamer beyond sensing small molecule and protein targets. For example, we think that this L-RNA version bi-functional FLAP approach should be generally applicable to other fluorogenic RNAs using achiral ligands,[36,37] and other nucleic acid structure-specific targeting L-Aptamers,[31–33,54–57] to detect and image targets not only in G4s, but also to other DNA/RNA structural motifs in the near future.

4. Conclusion

In this work, we have reported the original use of a low GC content library in G4-SELEX-seq, and developed a novel non-G4-contaning L-RNA aptamer, L-Apt.1-1, that can bind to *APP* rG4 with sub-nanomolar affinity. We revealed that the aptamer folds into a hairpin structure that does not contain G4 motif, and identified the key nucleotides and conditions that are essential for target recognition. Importantly, we demonstrated that L-Apt.1-1 has a strong binding preference toward *APP* rG4 against other non-intended targets, and has higher target specificity than the prior G4-containing L-RNA aptamer developed by us. We also showed that L-Apt.1-1 can reduce APP expression by binding to 3'UTR *APP* rG4. Lastly, we developed the first L-RNA-based fluorogenic bi-functional aptamer system, to light up rG4 structure in vitro and in cells. By using L-Apt.1-1_Pepper, we demonstrated the first nucleic acid-based approach to image an rG4 structure of interest (i.e., *APP* rG4). Our study demonstrated a new and important approach of developing non-G4-containing aptamer to target and image G4 of interest, and the tools developed can be further refined and applied for G4-mediated gene regulation and G4-imaging in cells.

5. Experimental Section

Oligonucleotides Preparation: DNA & RNA oligonucleotides were synthesized by Biosyntech, Genewiz, or Integrated DNA Technologies, and were stored at −20 °C in nuclease-free water.

G4-SELEX-Seq: G4-SELEX-seq started with the extension of a low GC ssDNA N_{30} random library with A:T:G:C ratio of 35%:35%:15%:15% to ds-DNA library. The ssDNA library (2 µM) was mixed with reverse primer (3 µM), 4 µL of 5× Li RT buffer, and dNTPs mix (100 mM Tris-HCl pH 7.5, 20 mM $MgCl_2$, 5 mM DTT, 750 mM LiCl, and 5 mM dNTPs) in nuclease-free water (19 µL), and heated at 95 °C for 5 min. After cooling down, 1 µL of 200 U µL^{-1} Superscript III reverse transcriptase (Thermo Fisher Scientific, USA) was added to the mixture and incubated at 50 °C for 50 min. The dsDNA library generated (100–150 ng) was then in vitro transcribed into N_{30} random RNA library with HiScribe T7 High Yield RNA Synthesis Kit (NEB, USA) with 40 µL volume, followed by the removal of DNA template by adding 2 µL TURBO DNase (Thermo Fisher Scientific, USA). Next, the transcribed RNAs were purified by a 10% denaturing PAGE and collected by using RNA clean and concentrator column (Zymo Research, USA). To prepare for selection, 75 µL of Dynabeads MyOne Streptavidin C1 at 10 mg mL^{-1} (Thermo Fisher Scientific, USA) was washed with 600 µL of solution A (100 mM NaOH and 50 mM NaCl) and 600 µL of solution B (100 mM NaCl), and resuspended in 75 µL of 2× selection buffer (150 mM KCl, 25 mM Tris-HCl pH 7.5, and 10 mM $MgCl_2$). Then, 0.75 µL of 10 mg mL^{-1} yeast tRNA (Thermo Fisher Scientific, USA) was added to the mixture with shaking at 700 rpm for 30–45 min at 25 °C using a thermo-shaker (Thermo Fisher Scientific, USA). After that, the RNA library pool with a final concentration of 4.5 µM was mixed with 2x RNA buffer (300 mM KCl and 50 mM Tris-HCl pH 7.5) to 50 µL, then refolded by heating at 95 °C and cooling on ice. Twenty-five microliters of tRNA pre-blocked beads were added and incubated at 700 rpm for 2 h. Afterward, the Dynabeads were discarded to remove non-specific binding RNAs. To start the positive selection, 5' biotin labeled *APP* L-rG4 (Biosyntech, China) was refolded by heating at 95 °C and cooling on ice, and mixed with the RNA pool with a final concentration of 0.65 µM. The resultant mixture was shaken at 300 rpm for 30 min for target binding. After that, the biotin-labeled *APP* L-rG4& RNA complexes were pulled down using 50 µL of beads, and washed with 600 µL of 1× selection buffer for five times. Lastly, target binding RNAs were eluted with 100 µL of elution buffer (25 mM NaOH and 1 mM EDTA), and neutralized by 50 µL of 1 M Tris-HCl immediately. The collected RNAs were then recovered to 30 µL using RNA clean and concentrator column. To generate ssDNA template from the selected RNAs by reverse transcription, the 30 µL purified RNA was mixed with reverse primer (0.33 µM), and heated at 95 °C for 5 min, then cooled down at 35 °C for 10 min. Then, 18 µL 5× Li RT buffer and 5 mM dNTPs mix, and 2 µL of 200 U µL^{-1} Superscript III RT were added, and diluted with nuclease-free water to 60 µL, and incubated at 50 °C for 15 min. The reaction was quenched by adding 0.6 µL of 10 M NaOH, and heated at 95 °C for 10 min to degrade the RNAs. After that, the resultant ssDNA was cooled to 25 °C, and neutralized by 15 µL of 1 M Tris-HCl pH 7.5. The reverse transcribed ssDNA was recovered to 30 µL using RNA clean and concentrator column and PCR amplified for next round selection. A small-scale PCR cycle test was carried out to decide the optimum number of cycles for large-scale DNA amplification. Forward primer and reverse primer (0.5 µM each), 8 µL of ssDNA, and 10 µL of 2× KAPA HiFi HotStart ReadyMix (Roche) were mixed to a total of 20 µL, and divided into five aliquots of 4 µL each. The aliquots were PCR amplified for 8, 10, 12, 14, and 16 cycles, respectively (3 min at 98 °C, (20 s at 98 °C, 20 s at 60 °C, 20 s at 72 °C)$_n$, 3 min at 72 °C, 4 °C). The optimum number of cycles was determined by the fewest PCR cycles that provide a clear band on an agarose gel stained by 6× DNA loading dye (NEB, USA) and SYBR Safe DNA Gel Stain (Thermo Fisher Scientific, USA). Lastly, the large-scale DNA amplification was carried out with 40 µL reaction volume with the same condition, and the dsDNA product was purified and collected using Zymoclean Gel DNA Recovery Kit (Zymo Research, USA). After five rounds of selection, the ds-DNAs were amplified for four cycles with NGS primers and dehydrated to vacuum concentration using Concentrator plus (Eppendorf) with a total of >200 ng. The dsDNAs were then submitted for NGS sequencing, and the results for two to five rounds were reported and analyzed in Microsoft Excel.

G4 Prediction for Aptamer Candidates: G4 prediction analysis was performed by using G4RNAscreener v.0.3 (http://scottgroup.med.usherbrooke.ca/G4RNA_screener/) with a default setting of G4H (G4Hunter) > 0.9 and G4NN (G4 Neural Network) > 0.5 as G4 threshold.

Electrophoretic Mobility Shift Assay (EMSA): Fourfold serial dilution was performed for D- or L-Apt.1-1 with an initial concentration of 8 µM to generate 12 sets of the sample solution in selection buffer containing 25 mM Tris-HCl (pH 7.5), 150 mM KCl, 1 mM $MgCl_2$, with the addition of 8% glycerol or sucrose solution and 20 nM 5' FAM labeled *APP* L- or D-rG4. The aptamer solutions were refolded by heating at 95 °C and cooling on ice, then mixed with *APP* rG4 and incubated at 37 °C for 30 min. The solutions were then loaded to 10% native non-denaturing gel in 50 mM potassium acetate, 25 mM Tris-HCl pH 7.5, and 1 mM $MgCl_2$ buffer,

and conducted at 70 mA for 50 min at 4 °C. The binding was visualized by scanning the gel in Amersham TYPHOON Imager (Cytiva), followed by gel image quantification and analysis using ImageJ (National Institutes of Health, USA) and GraphPad Prism (GraphPad Software Inc.). For magnesium ion dependence, all conditions were the same except for $MgCl_2$ concentration (0 and 2 mM). For potassium and sodium ion dependence, all conditions were the same except for KCl concentrations (0, 50, 100, and 200 mM) and NaCl concentration (150 mM). For binding test, sample solutions containing 0, 20, 200, and 2000 nM aptamer candidates and 10 nM 5' FAM labeled D-target were prepared, and other procedures were the same. For mutagenesis analysis, sample solutions containing 100 nM D-Apt.1-1 wildtype and mutant, and 10 nM 5' FAM labeled *APP* L-rG4 were prepared, and other procedures were the same. For binding specificity, sample solutions containing 100 nM L-Apt.1-1 and 5/10 nM 5' FAM labeled D-target were prepared, and other procedures were the same. For the binding test using cell lysate, all conditions were the same with the addition HeLa cell lysate.

Circular Dichroism Spectroscopy: Sample solutions containing 5 µM D-Apt.1-1, 10 mM LiCac pH 7.0, and 150 mM KCl or LiCl were prepared, and were refolded by heating at 95 °C and cooled on ice. Samples were vortexed and spun down before transferring to the quartz cuvette and scanned two times at 25 °C within 220 and 310 nm by using J-1500 Circular Dichroism spectrophotometer (Jasco, Japan). The data was obtained in every 1 nm with 0.5 s nm^{-1} responding time, and were normalized and smoothed over 5 nm in Microsoft Excel, and plotted using GraphPad Prism.

G4-Ligand Enhanced Fluorescence Assay: Sample solutions containing 1 µM D-Apt.1-1, 10 mM LiCac pH 7.0, 150 mM KCl/LiCl were prepared, and were refolded by heating at 95 °C and cooling on ice. Thioflavin T (ThT) or *N*-methyl mesoporphyrin IX (NMM) ligands were added to the solutions and transferred to the quartz cuvette. The excitation wavelengths were 425 and 394 nm for ThT and NMM, respectively, and the emission fluorescence was measured in the range of 440–700 nm for ThT and 550–750 nm for NMM at 25 °C using HORIBA FluoroMax-4 Fluorometer. The experiment was conducted with 5 nm entrance slit, 2 nm exit slit, and 2 nm increment. The data were then processed using Microsoft Excel and plotted using GraphPad Prism.

Biostability Assay: Sample solutions containing 100 nM D- or L-Apt.1-1 were refolded in selection buffer by heating at 95 °C and cooling on ice, then incubated at 25 °C for 2 h. In the period, 10 ng μL^{-1} RNase A or 5% FBS was added to each sample solution at 0 min and every 30 min, respectively. The RNAs were then visualized by a 10% denaturing PAGE with SYBR Gold Nucleic Acid Gel Stain (Thermo Fisher Scientific, USA), scanned in ChemiDoc Touch imaging system (Bio-Rad). Gel image quantification and analysis were done by using ImageJ (National Institutes of Health, USA) and GraphPad Prism (GraphPad Software Inc.).

Cell Counting Kit-8 (CCK-8) Cytotoxicity Assay: A total of 6×10^4 per well of HeLa cells were seeded into a 96-well plate. After 24h, cells were transfected with different concentrations of L-Apt.1-1 (0, 25, 50, and 100 nM) using Lipofectamine 2000 (Thermo Fisher Scientific). At 48 h post-transfection, cells were replaced with fresh medium and 10% CCK-8 (MedChemExpress) was added and incubated at 37 °C for 1.25h. Then, the absorbance at 450 nm was measured using a microplate reader (SpectraMax iD5 Multi-Mode Microplate Reader). The cell survival rate was calculated.

Western Blotting: A total of 1×10^5 per well HeLa cells were seeded onto a 24-well plate, respectively. The next day, cells were transfected with different concentrations of L-Apt.1-1 or D-Apt.1-1 by Lipofectamine 2000 (Thermos Fisher Scientific). After ≈48 h post-transfection, cells were harvested and lysed in TritonX-100 lysis buffer (50 mM Tris-HCl pH 7.5, 1% TritonX-100, 250 mM NaCl, 5 mM EDTA) supplemented with Halt Protease Inhibitor Cocktail (Thermos Fisher Scientific). Cell lysates were centrifuged at 16 000 × *g* for 10 min at 4 °C and the supernatants were boiled with Laemmli Sample Buffer (Bio-Rad) for 10 min. Then samples were resolved by 8% SDS-PAGE and transferred to PVDF membrane. Blocking was done by incubating the membrane with 5% milk in TBST for 1 h with rotation. Then the membrane and the primary antibody (APP, Millipore Sigma MAB348, 1:1000) (GAPDH, Santa Cruz Biotechnology sc-32233, 1:1000) were mixed and shaken for 1 h. Then the membrane was washed four times using TBST with rotation, 8 min each time. After that, HRP conjugated secondary antibody was added to the membrane and shaken for 1 h. After four times washing with TBST, 5 min each time, the membrane was treated with ECL substrates and scanned by ChemiDoc Touch imaging system (Bio-Rad). Protein band intensity was then analyzed by the Image Lab 5.2.1 software (Bio-Rad).

Quantitative Reverse Transcription-Polymerase Chain Reaction (qRT-PCR): Total RNAs were extracted using RNase Plus Mini Kit (Qiagen) according to the manufacturer's instructions. 80 ng of total RNAs were reverse transcribed to cDNA using PrimeScript RT Master Mix (Perfect Real Time) (Takara). For qRT-PCR detection, TB Green Premix Ex Taq (Tli RNase H Plus) (Takara) was used together with primers of *APP* and *GAPDH* separately. *GAPDH* was an internal control. All qRT-PCRs were tested on the machine CFX connect real-time system (Bio-Rad). Relative mRNA level of *APP* was obtained from normalization by *GAPDH*. The primers used are shown in Table S1 (Supporting Information).

Characterization of Apt.1-1_Pepper: Samples containing 0.5 µM D- or L-Apt.1-1_Pepper were refolded by heating at 95 °C and cooling on ice in selection buffer, various concentrations of L- or D-rG4 were then added and incubated at 37 °C for 30 min, respectively. Then, 1 µM HBC530 (TargetMol, China) was added and incubated at 37 °C for 15 min. Sample solutions were loaded into 384 well black plate and scanned with SpectraMax iD5 Multi-Mode Microplate Reader (Molecular Devices, USA) with excitation at 455 nm and emission at 495–650 nm. The data was then processed using Microsoft Excel and plotted using GraphPad Prism.

Cell Imaging of APP rG4 Using L-Apt.1-1_Pepper: A total of 2.5×10^4 HeLa or HEK293T cells were seeded onto a 35 mm confocal dish for 24 h. Next day, TAMRA-wt/mut *APP* rG4 motif oligo was refolded in selection buffer containing 25 mM Tris-HCl (pH 7.5), 150 mM KCl, 1 mM $MgCl_2$, by heating at 95 °C and cooling at 25 °C for 5 min and at 4 °C for at least 5 min, respectively. Then HeLa cells were transfected with 200 nM refolded TAMRA-wt/mut *APP* rG4 motif oligo, while HEK293T cells were with 100 nM oligos, respectively using Lipofectamine 2000. After ≈18h, cells were washed with phosphate-buffered saline (PBS) for one time, fixed with 4% paraformaldehyde at 25 °C for 15 min, and washed with 2× Saline Sodium Citrate (SSC) or PBS for five times. Then cells were permeabilized by 0.5% Triton X-100 at 37 °C for 30 min and washed with 2× SSC four times. L-Apt.1-1_Pepper was refolded in buffer containing 25 mM Tris-HCl (pH 7.5), 150 mM KCl, 5 mM $MgCl_2$, by heating at 95 °C for 5 min, and cooling at 4 °C for 5 min. Then 500 nM refolded L-Apt.1-1_Pepper and 2 µM HBC530 were added to the dish in stain buffer containing 30% formamide, 10% dextran sulfate, 2.4× SSC, 5 mM $MgCl_2$, to stain cells overnight at 37 °C. Next day, cells were washed with 2× SSC five times and stained with 5 µg mL^{-1} Hoechst 33342 overnight at room temperature. At last, cells were scanned by confocal microscopy (Leica SPE). The percentage of colocalized green and red was calculated and processed using Microsoft Excel.

Statistical Analysis: For the K_d analysis,

$$\text{Fraction bound} = \frac{\text{bound} - \text{background}}{(\text{bound} - \text{background}) + (\text{unbound} - \text{background})} \quad (1)$$

The fraction bound values and concentrations of aptamer used were input to GraphPad Prism for generation of K_d values using "one site–specific binding".

For Circular dichroism spectroscopy analysis,

$$\text{Signal } (\varepsilon) = \frac{(\text{aptamer} - \text{buffer}) \times 30 \times 1 \times 0.000005}{32980} \quad (2)$$

The signal (ϵ) was smoothed over 5 nm.

For G4-ligand enhanced fluorescence assay analysis,

$$\text{Signal} = \text{aptamer} - \text{buffer} \quad (3)$$

For biostability assay analysis,

$$\text{Fraction retained} = \frac{\text{band (X min)} - \text{background}}{\text{band (0 min)} - \text{background}} \quad (4)$$

For cell counting Kit-8 (CCK-8) cytotoxicity assay analysis,

$$\text{Cell survival rate} = \frac{\text{A450 (x nM aptamer)} - \text{A450 (blank)}}{\text{A450 (0 nM aptamer)} - \text{A450 (blank)}} \times 100 \quad (5)$$

For western blotting analysis,

$$\text{Relative intensity} = \frac{\text{adjusted volume of APP}}{\text{adjusted volume of GAPDH}} \quad (6)$$

For qRT-PCR analysis,

$$\text{Relative } \textit{APP} \text{ mRNA level} = 2^{-(\Delta\Delta Cq)} \quad (7)$$

$$\Delta Cq = Cq\ (\textit{APP}) - Cq\ (\text{GAPDH}) \quad (8)$$

$$\Delta\Delta Cq = \Delta Cq\ (\text{x nM aptamer}) - \Delta Cq\ (\text{0 nM aptamer}) \quad (9)$$

For Apt.1-1_Pepper in vitro assays analysis,

$$\text{Fold effect} = \frac{\text{pepper } (+\textit{APP}) - \text{blank}}{\text{pepper } (-\textit{APP}) - \text{blank}} \quad (10)$$

For Cell imaging using L-Apt.1-1_Pepper,

$$\text{Foci Ratio of colocalization} = \frac{\text{overlap foci of Green and Red}}{\text{Red foci}} \quad (11)$$

The sample size (n) used in HeLa cells was 750 foci for wt group and 1000 foci for mut group, while 450 foci for wt/mut groups was used in HEK293T cells.

Values were obtained from three replicates and error bars display standard error of mean. Statistical methods *t*-test was used, $*p < 0.05$, meaning statistical significance. NS, not significance. Band intensities were collected using ImageJ. Calculations were done using Microsoft Excel. Graphs and spectrum were generated using GraphPad Prism.

Supporting Information

Supporting Information is available from the Wiley Online Library or from the author.

Acknowledgements

H.-L.L. and H.Z. contributed equally to this work. The authors thank Kwok lab members who provided support in this project. This work was supported by the NSFC Excellent Young Scientists Fund (Hong Kong and Macau) Project [32222089]; Research Grants Council of the Hong Kong SAR, China Projects [CityU 11100123, CityU 11100222, CityU 11100421]; Croucher Foundation Project [9509003]; State Key Laboratory of Marine Pollution Seed Collaborative Research Fund [SCRF/0037, SCRF/0040, SCRF/0070]; City University of Hong Kong projects [7030001, 6000827, 9678302] to C.K.K.

Conflict of Interest

The authors declare no conflict of interest.

Data Availability Statement

The data that support the findings of this study are available in the supplementary material of this article.

Keywords

amyloid precursor protein (APP), aptamer, gene regulation, G-quadruplex, nucleic acids

Received: July 17, 2024
Revised: August 6, 2024
Published online: September 3, 2024

[1] C. K. Kwok, C. J. Merrick, *Trends Biotechnol.* **2017**, *35*, 997.
[2] C. K. Kwok, G. Marsico, S. Balasubramanian, *Cold Spring Harb. Perspect.* **2018**, *10*, a032284.
[3] K. Lyu, E. Y. Chow, X. Mou, T. F. Chan, C. K. Kwok, *Nucleic Acids Res.* **2021**, *49*, 5426.
[4] S. Millevoi, H. Moine, S. Vagner, *Wiley Interdiscip Rev RNA* **2012**, *3*, 495.
[5] D. Rhodes, H. J. Lipps, *Nucleic Acids Res.* **2015**, *43*, 8627.
[6] M. M. Fay, S. M. Lyons, P. Ivanov, *J. Mol. Biol.* **2017**, *429*, 2127.
[7] P. Kharel, S. Balaratnam, N. Beals, S. Basu, *Wiley Interdiscip Rev RNA* **2020**, *11*, e1568.
[8] D. Varshney, J. Spiegel, K. Zyner, D. Tannahill, S. Balasubramanian, *Nat. Rev. Mol. Cell. Biol.* **2020**, *21*, 459.
[9] C. K. Kwok, G. Marsico, A. B. Sahakyan, V. S. Chambers, S. Balasubramanian, *Nat. Methods* **2016**, *13*, 841.
[10] E. Crenshaw, B. P. Leung, C. K. Kwok, M. Sharoni, K. Olson, N. P. Sebastian, S. Ansaloni, R. Schweitzer-Stenner, M. R. Akins, P. C. Bevilacqua, A. J. Saunders, *PLoS One* **2015**, *10*, 0143160.
[11] K. Lyu, S. B. Chen, C. Y. Chan, J. H. Tan, C. K. Kwok, *Chem. Sci.* **2019**, *10*, 11095.
[12] B. De Strooper, E. Karran, *Cell* **2016**, *164*, 603.
[13] J. M. Long, D. M. Holtzman, *Cell* **2019**, *179*, 312.
[14] Y. Guo, Q. Wang, S. Chen, C. Xu, *Metabolism* **2021**, *115*, 154454.
[15] D. S. Knopman, H. Amieva, R. C. Petersen, G. Chetelat, D. M. Holtzman, B. T. Hyman, R. A. Nixon, D. T. Jones, *Nat. Rev. Dis. Primers* **2021**, *7*, 33.
[16] Y. Cho, H. G. Bae, E. Okun, T. V. Arumugam, D. G. Jo, *Pharmacol. Ther.* **2022**, *235*, 108122.
[17] Y. H. Wang, Q. F. Yang, X. Lin, D. Chen, Z. Y. Wang, B. Chen, H. Y. Han, H. D. Chen, K. C. Cai, Q. Li, S. Yang, Y. L. Tang, F. Li, *Nucleic Acids Res.* **2022**, *50*, D150.
[18] V. Sanchez-Martin, M. Soriano, J. A. Garcia-Salcedo, *Cancers (Basel)* **2021**, *13*.
[19] M. I. Umar, D. Ji, C. Y. Chan, C. K. Kwok, *Molecules* **2019**, *24*.
[20] G. Biffi, D. Tannahill, J. McCafferty, S. Balasubramanian, *Nat. Chem.* **2013**, *5*, 182.
[21] G. Biffi, M. Di Antonio, D. Tannahill, S. Balasubramanian, *Nat. Chem.* **2014**, *6*, 75.
[22] S. Galli, L. Melidis, S. M. Flynn, D. Varshney, A. Simeone, J. Spiegel, S. K. Madden, D. Tannahill, S. Balasubramanian, *J. Am. Chem. Soc.* **2022**, *144*, 23096.
[23] M. I. Umar, C. Y. Chan, C. K. Kwok, *Nat. Protoc.* **2022**, *17*, 1385.
[24] G. Zhu, X. Chen, *Adv Drug Deliv Rev* **2018**, *134*, 65.
[25] D. Ji, H. Feng, S. W. Liew, C. K. Kwok, *Trends Biotechnol.* **2023**, *41*, 1360.
[26] R. Oliveira, E. Pinho, A. L. Sousa, J. J. DeStefano, N. F. Azevedo, C. Almeida, *Trends Biotechnol.* **2022**, *40*, 549.
[27] A. Vater, S. Klussmann, *Drug Discov Today* **2015**, *20*, 147.
[28] B. E. Young, N. Kundu, J. T. Sczepanski, *Chemistry* **2019**, *25*, 7981.
[29] A. Nolte, S. Klussmann, R. Bald, V. A. Erdmann, J. P. Furste, *Nat. Biotechnol.* **1996**, *14*, 1116.
[30] S. Klussmann, A. Nolte, R. Bald, V. A. Erdmann, J. P. Furste, *Nat. Biotechnol.* **1996**, *14*, 1112.

[31] C. Y. Chan, C. K. Kwok, *Angew. Chem., Int. Ed.* **2020**, *59*, 5293.
[32] M. I. Umar, C. K. Kwok, *Nucleic Acids Res.* **2020**, *48*, 10125.
[33] H. Zhao, H. Y. Wong, D. Ji, K. Lyu, C. K. Kwok, *ACS Appl. Mater. Interfaces* **2022**, *14*, 30582.
[34] M. You, S. R. Jaffrey, *Annu. Rev. Biophys.* **2015**, *44*, 187.
[35] R. J. Trachman 3rd, L. Truong, A. R. Ferre-D'Amare, *Trends Pharmacol. Sci.* **2017**, *38*, 928.
[36] L. Truong, A. R. Ferre-DAmare, *Protein Sci.* **2019**, *28*, 1374.
[37] H. M. Zhou, S. J. Zhang, *Crit. Rev. Anal. Chem.* **2022**, *52*, 1644.
[38] J. S. Paige, K. Y. Wu, S. R. Jaffrey, *Science* **2011**, *333*, 642.
[39] E. V. Dolgosheina, S. C. Jeng, S. S. Panchapakesan, R. Cojocaru, P. S. Chen, P. D. Wilson, N. Hawkins, P. A. Wiggins, P. J. Unrau, *ACS Chem. Biol.* **2014**, *9*, 2412.
[40] G. S. Filonov, J. D. Moon, N. Svensen, S. R. Jaffrey, *J. Am. Chem. Soc.* **2014**, *136*, 16299.
[41] W. Song, G. S. Filonov, H. Kim, M. Hirsch, X. Li, J. D. Moon, S. R. Jaffrey, *Nat. Chem. Biol.* **2017**, *13*, 1187.
[42] C. Steinmetzger, N. Palanisamy, K. R. Gore, C. Hobartner, *Chemistry* **2019**, *25*, 1931.
[43] X. Chen, D. Zhang, N. Su, B. Bao, X. Xie, F. Zuo, L. Yang, H. Wang, L. Jiang, Q. Lin, M. Fang, N. Li, X. Hua, Z. Chen, C. Bao, J. Xu, W. Du, L. Zhang, Y. Zhao, L. Zhu, J. Loscalzo, Y. Yang, *Nat. Biotechnol.* **2019**, *37*, 1287.
[44] K. Huang, X. Chen, C. Li, Q. Song, H. Li, L. Zhu, Y. Yang, A. Ren, *Nat. Chem. Biol.* **2021**, *17*, 1289.
[45] H. C. Rees, W. Gogacz, N. S. Li, D. Koirala, J. A. Piccirilli, *ACS Chem. Biol.* **2022**, *17*, 1866.
[46] Q. Wang, F. Xiao, H. Su, H. Liu, J. Xu, H. Tang, S. Qin, Z. Fang, Z. Lu, J. Wu, X. Weng, X. Zhou, *Nucleic Acids Res.* **2022**, *50*, e84.
[47] M. Fang, H. Li, X. Xie, H. Wang, Y. Jiang, T. Li, B. Zhang, X. Jiang, Y. Cao, R. Zhang, D. Zhang, Y. Zhao, L. Zhu, X. Chen, Y. Yang, *Biosens. Bioelectron.* **2023**, *235*, 115411.
[48] Z. Chen, W. Chen, Z. Reheman, H. Jiang, J. Wu, X. Li, *Nucleic Acids Res.* **2023**, *51*, 8322.
[49] M. Zuker, *Nucleic Acids Res.* **2003**, *31*, 3406.
[50] J. M. Garant, J. P. Perreault, M. S. Scott, *Biochimie* **2018**, *151*, 115.
[51] A. Bedrat, L. Lacroix, J. L. Mergny, *Nucleic Acids Res.* **2016**, *44*, 1746.
[52] J. M. Garant, J. P. Perreault, M. S. Scott, *Bioinformatics* **2017**, *33*, 3532.
[53] P. Yin, M. Ge, S. Xie, L. Zhang, S. Kuang, Z. Nie, *Chem. Sci.* **2023**, *14*, 14131.
[54] J. T. Sczepanski, G. F. Joyce, *J. Am. Chem. Soc.* **2013**, *135*, 13290.
[55] J. T. Sczepanski, G. F. Joyce, *J. Am. Chem. Soc.* **2015**, *137*, 16032.
[56] S. Dey, J. T. Sczepanski, *Nucleic Acids Res.* **2020**, *48*, 1669.
[57] D. Ji, J. H. Yuan, S. B. Chen, J. H. Tan, C. K. Kwok, *Nucleic Acids Res.* **2023**, *51*, 11439.

